







Simultaneous Constraints on the Mass and Radius of Aql X–1 from Quiescence and X-Ray Burst Observations

Zhaosheng Li^{1,2,3} , Maurizio Falanga² , Li Chen⁴, Jinlu Qu⁵ , and Renxin Xu^{6,7,8} 

¹Department of Physics, Xiangtan University, Xiangtan, 411105, P.R. China; lizhaosheng@xtu.edu.cn

²International Space Science Institute, Hallerstrasse 6, 3012 Bern, Switzerland

³Albert Einstein Center for Fundamental Physics, Institute for Theoretical Physics/Laboratory for High-Energy Physics, University of Bern, Switzerland

⁴Department of Astronomy, Beijing Normal University, Beijing 100875, China

⁵Laboratory for Particle Astrophysics, Institute of High Energy Physics, CAS, Beijing 100049, P.R. China

⁶Kavli Institute for Astronomy and Astrophysics, Peking University, Beijing 100871, P.R. China

⁷School of Physics and State Key Laboratory of Nuclear Physics and Technology, Peking University, Beijing 100871, P.R. China

Received 2016 March 5; revised 2017 June 23; accepted 2017 June 29; published 2017 August 4

Abstract

The measurement of neutron star mass and radius is one of the most direct ways to distinguish between various dense matter equations of state. The mass and radius of accreting neutron stars hosted in low-mass X-ray binaries can be constrained by several methods, including photospheric radius expansion from type I X-ray bursts and from quiescent spectra. In this paper, we apply for the first time these two methods simultaneously to constrain the mass and radius of Aql X–1. The quiescent spectra from *Chandra* and *XMM-Newton*, and photospheric radius expansion bursts from *RXTE* are used. The determination of the mass and radius of Aql X–1 is also used to verify the consistency between the two methods and to narrow down the uncertainties of the neutron star mass and radius. It is found that the distance to Aql X–1 should be in the range of 4.0–5.75 kpc, based on the overlapping confidence regions between photospheric radius expansion burst and quiescent spectra methods. In addition, we show that the mass and radius determined for the compact star in Aql X–1 are compatible with strange star equations of state and conventional neutron star models.

Key words: equation of state – stars: neutron – X-rays: binaries – X-rays: bursts – X-rays: individual (Aql X–1)

1. Introduction

Accurate measurements of neutron star (NS) masses and radii provide the tightest constraints on the equations of state (EOSs) of these objects, i.e., the relation between the pressure and the supranuclear density in their interiors (Lattimer 2012). NS masses can be determined in low- or high-mass X-ray binary systems hosting a main-sequence companion star, or with high accuracy in double NSs or NS–white dwarf systems, through their mass functions or pulse arrival time, respectively (see, e.g., Taylor 1992; Weisberg et al. 2010; Watts et al. 2015). However, the precise and contemporaneous measurements of NS masses and radii (mass–radius ratio) are still challenging (see, e.g., Miller & Lamb 2016, and references therein).

Several methods have been proposed to constrain NS masses and radii, e.g., using type I X-ray bursts exhibiting photospheric radius expansion (PRE; see Section 1.1) (Sztajno et al. 1987), modeling thermal emission from quiescent low-mass X-ray binaries (qLMXBs; see Section 1.2) (Heinke et al. 2006), modeling the X-ray pulse profile of accreting millisecond X-ray pulsars (see, e.g., Poutanen & Gierliński 2003), or measuring the gravitational redshift of spectral features produced in the NS photosphere (Özel 2006). The gravitational redshift provides one of the most accurate and model-independent methods to obtain the NS mass–radius ratio. Currently, a debated measurement of a large gravitational redshift measurement, $z = 0.35$, was claimed for absorption lines in the X-ray burst spectra of the NS EXO 0748–676 (Cottam et al. 2002), but the results were not confirmed in subsequent publications (Sidoli et al. 2005; Cottam et al. 2008).

LMXB systems, hosting an X-ray pulsar, accrete matter via Roche lobe overflow from a main-sequence donor star ($M < 1 M_{\odot}$), forming a disk around the compact object. The accreted matter is channeled by the magnetic field lines toward the magnetic poles, which produce by impact two hot spots on the NS surface. Therefore, when the NS spins, the observed X-ray pulses are modulated by relativistic effects (e.g., light bending, Doppler boosting, aberration), which depend on the compactness term M/R (Pechenick et al. 1983). Modeling the pulse profiles from X-ray pulsars can provide strong constraints on the NS mass and radius, although some degeneracies due to unknown factors like the geometry of the hot spot and the observer inclination have to be taken account (see, e.g., Beloborodov 2002; Poutanen & Gierliński 2003; Leahy 2004; Bogdanov et al. 2007; Leahy et al. 2009). To break the degeneracies among various parameters and to quantify the mass and radius simultaneously, Psaltis et al. (2014) utilized the properties of the fundamental and the second harmonic of the pulse profile. However, a larger number of processes should be considered, such as the oblateness of the NS surface, the quadrupole moment, the pulse profile variation, the geometrical factors, and the NS atmosphere emission (Morsink et al. 2007; Hartman et al. 2008; Psaltis & Özel 2014; Psaltis et al. 2014; Bauböck et al. 2015). Considering these effects, the *Neutron Star Interior Composition Explorer* mission, launched on 2017 June 3, is designed to determine at 10% of accuracy the NS radius from X-ray pulsars (Gendreau et al. 2012). If a pulse profile of an X-ray pulsar shows long time evolution, implying that the hot spots are drifting on the NS surface, then large-area detectors are needed to collect enough photons on short timescales (Zhang et al. 2016).

⁸ FAST Fellow distinguished.

1.1. NS Mass–Radius Relation from Type I X-Ray Bursts with PRE

The accreted matter on an NS surface can trigger hydrogen/helium or mixed thermonuclear flashes, called type I X-ray bursts (see, e.g., Lewin et al. 1993). The total burst energy released is on the order of $\sim 10^{39-42}$ erg, and the spectra are described by a blackbody with a temperature kT_{bb} and its normalization K (e.g., Galloway et al. 2008). The energy-dependent decay time of these bursts is attributed to the cooling of the NS photosphere and results in a gradual softening of the burst spectrum (see Lewin et al. 1993; Strohmayer & Bildsten 2006, for a review). During some type I X-ray bursts, the energy release is high enough that the luminosity reaches the Eddington limit, $L_{\text{Edd}} \sim 2 \times 10^{38}$ erg s $^{-1}$, i.e., the value at which the gravity balances the radiative pressure. At that luminosity level, the radiation pressure lifts the surface layers from the NS in a PRE episode. Since the luminosity scales as $L_{\text{burst}} \propto R_{\text{bb}}^2 (kT_{\text{bb}})^4$ for pure blackbody spectrum, during the PRE episode, while the bolometric luminosity remains constant at the Eddington value, the temperature, kT_{bb} , drops when the radius of the photosphere, R_{bb} , expands. The point at which the NS atmosphere reaches the surface again, $R_{\text{bb},\text{min}} = R_{\text{NS}}$, i.e., at the highest temperatures, is called *touchdown*. To derive the bolometric burst flux, a color correction factor, $f_c = T_{\text{bb}}/T_{\text{eff}}$, should be applied, since the burst-emitted photons are upscattered in a hot NS atmosphere (Ebisuzaki et al. 1984).

Assuming spherically symmetric emission from a nonspinning NS surface, the Eddington luminosity is expressed as (Lewin et al. 1993)

$$L_{\text{Edd}} = 4\pi D^2 F_{\text{TD}} = \frac{4\pi G M c}{\kappa_{\text{es}} D^2} \left(1 - \frac{2GM}{Rc^2}\right)^{1/2}, \quad (1)$$

where G is the gravitational constant, c is the speed of light, D is the distance to the source, and M and R are the NS mass and radius, respectively. The parameter $\kappa_{\text{es}} = 0.2(1 + X)$ is the electron scattering opacity, X is the atmosphere’s hydrogen mass fraction ($X = 1$ is for pure hydrogen), and F_{TD} is the Eddington flux at the touchdown. After the touchdown moment, the NS photosphere cools down on the whole surface, while the emission area remains nearly constant. This has been observed in a substantial fraction of X-ray bursts (Güver et al. 2012). Given the distance to the source, the blackbody normalization can be written as (Özel 2006)

$$K = \frac{1}{f_c^4} \frac{[R(1+z)]^2}{D^2} = (f_c A)^{-4}, \quad (2)$$

where $A = (R(1+z)/D)^{-1/2}$ is the apparent angular size, $1+z = (1 - 2GM/Rc^2)^{-1/2}$, and z is the gravitational redshift. Therefore, the NS mass and radius can be constrained from the observed K and F_{TD} , once the atmosphere’s hydrogen mass fraction, X , the color correction factor, f_c , and the source distance are known. We note that this “touchdown” method assumes that the color correction factor is constant during the whole burst cooling phase. However, based on NS hot atmosphere models, while the emission approaches the Eddington limit, the color correction factor rises rapidly (Suleimanov et al. 2011, 2012). In this case, the $F-K^{-1/4}$ track denotes the dependence between f_c and the flux; afterward, the F_{Edd} and A are fitted from the $F-K^{-1/4}$ curve

to estimate the NS mass and radius. This is the so-called “cooling tail” method. A study of 4U 1608–52 showed that the $F-K^{-1/4}$ curves follow the theoretical atmosphere model only if the source is in a low accretion (or hard) state (Poutanen et al. 2014). Therefore, to constrain the mass and radius following the predicted cooling tail shape, the authors of this work proposed to study only PRE bursts occurring during a hard spectral state (Suleimanov et al. 2011, 2012). This is in contradiction to the results published by Özel et al. (2015) that the mass and radius of 4U 1608–52 are best determined using bursts with the brightest touchdown. It is challenging, for some bursts, to follow the very steep cooling tail after touchdown, as the limited time resolution of *RXTE* could not resolve the blackbody normalization evolution at these phases (Özel et al. 2015).

For an NS atmosphere model, considering the energy-dependent Klein–Nishina cross section, the Eddington luminosity, Equation (1), can be rewritten as (see Özel et al. 2016, and references therein)

$$F_{\text{TD}} = \frac{GMc}{\kappa_{\text{es}} D^2} \left(1 - \frac{2GM}{Rc^2}\right)^{1/2} \times \left[1 + \left(\frac{kT_{\text{TD}}}{38.8 \text{ keV}}\right)^{a_g} \left(1 - \frac{2GM}{Rc^2}\right)^{-a_g/2}\right], \quad (3)$$

where T_{TD} is the critical temperature at the Eddington limit during touchdown, and $a_g = 1.01 + 0.067(g_{\text{eff}}/10^{14} \text{ cm s}^{-2})$, with $g_{\text{eff}} = GMR^{-2}(1 - 2GM/Rc^2)^{-1/2}$ being the effective gravitational acceleration constant. The blackbody normalization, Equation (2), can be rewritten considering the Doppler spectrum broadening, the oblateness, and the NS quadrupole moment with spin frequencies larger than $\nu_{\text{NS}} = 400$ Hz (Bauböck et al. 2015; Özel et al. 2016):

$$K = \frac{R^2}{D^2 f_c^4} \left(1 - \frac{2GM}{Rc^2}\right)^{-1} \left\{1 + \left[0.108 - 0.096 \frac{M}{M_{\odot}}\right] - \left(0.061 - 0.114 \frac{M}{M_{\odot}}\right) \frac{R}{10 \text{ km}} - 0.128 \left(\frac{R}{10 \text{ km}}\right)^2 \left[\left(\frac{\nu_{\text{NS}}}{10^3 \text{ Hz}}\right)^2\right]^2\right\}. \quad (4)$$

Given the large number of parameters to determine the NS mass and radius, two different distribution probability approaches have been introduced, i.e., the Bayesian and frequentist (Özel et al. 2009, 2015). For a given pair of NS mass and radius (M, R), the equation of the Bayesian probability to obtain the observed touchdown flux, F_{TD} , and blackbody normalization, K , is

$$P(\text{data}|M, R) = \int P(D) dD \int P(f_c) df_c \int P(kT_{\text{TD}}) dkT_{\text{TD}} \times \int P(X) dX P[F_{\text{TD}}(M, R, D, X, kT_{\text{TD}})] \times P[K(M, R, D, f_c)]. \quad (5)$$

The frequentist approach differs from the Bayesian approach by an additional term, i.e., the Jacobian factor $J = 2cGR|1 - 4GM/Rc^2|/D^2 f_c^2 \kappa_{\text{es}}(1 - 2GM/Rc^2)^{3/2}$ (Özel et al. 2015).

The Jacobian factor is equal to zero for $R = 4GM/c^2$ in the M – R plane, leading to two separated M – R solutions. If the inferred M – R values are close to the $R = 4GM/c^2$ separation line, the NS M – R values are biased. At variance, for the Bayesian approach method, if the M/R values approach the $R = 4GM/c^2$ line, one solution exists. We thus choose to constrain the mass and radius of Aql X–1 adopting the Bayesian approach (Özel et al. 2015, 2016).

For the touchdown method, we constrain the NS M – R values using Equations (3)–(5) and by taking into account the source distance, atmosphere composition, touchdown flux and temperature, blackbody normalization, and color correction factor uncertainties. Following Özel et al. (2016), we consider blackbody normalization values in the range (0.1–0.7) F_{TD} . The upper value is chosen to overcome the potential missing touchdown moment, and the lower value is set to avoid a partial emission, occurring in case the cooling luminosity becomes so faint that it may lead to an underestimated blackbody normalization. Moreover, for the selected blackbody normalization range, f_c is nearly invariant for several hot atmosphere models with different metal abundances and surface gravities (see, e.g., Madej et al. 2004; Majczyna et al. 2005; Suleimanov et al. 2011, 2012).

1.2. NS Mass–Radius Relation from Quiescent Spectra

The spectrum of qLMXBs can be modeled by two components: a soft thermal component together with a hard nonthermal component (Rutledge et al. 2001a). We note that for most of the qLMXBs in the globular cluster the emission spectrum is dominated by a soft thermal emission with a weak or nonexistent nonthermal component (Guillot et al. 2013). The soft thermal component is interpreted as being due to deep crustal heating, mainly emitted throughout the NS atmosphere (Brown et al. 1998). NS masses and radii can thus be predicted by fitting the qLMXB spectra with atmosphere models, e.g., NSATMOS (Heinke et al. 2006), NSA (Zavlin et al. 1996), or MCPHAC (Haakonsen et al. 2012) (Heinke et al. 2006; Webb & Barret 2007; Guillot et al. 2011, 2013; Guillot & Rutledge 2014; Bogdanov et al. 2016). In all these models a pure hydrogen atmosphere is assumed unless a hydrogen-deficit companion star is observed, by, e.g., measuring an upper limit of the $H\alpha$ line equivalent width (Heinke et al. 2014).

The knowledge of the hard spectrum is critical, since the hard component may affect the soft spectrum during the simultaneous fit. The hard component is usually interpreted as being due to residual accretion (Rutledge et al. 2001a; Campana et al. 2004; Cackett et al. 2010; Bernardini et al. 2013; Chakrabarty et al. 2014), or emission from either a boundary layer (where the accretion flow hits the NS surface) or a radiatively inefficient accretion flow model (Chakrabarty et al. 2014; D’Angelo et al. 2015).

For Cen X–4, X-ray flares have been observed during the quiescent state, where the hard X-ray photons (2–10 keV) are positively correlated with the soft X-ray photons (0.3–2.0 keV). The total X-ray spectrum is correlated with the ultraviolet and optical disk emission (Cackett et al. 2010; Bernardini et al. 2013; Coti Zelati et al. 2014). Therefore, the total X-ray emission from Cen X–4 may arise solely from a continuous and variable low-level accretion flow (e.g., Zampieri et al. 1995, 2001). This interpretation excludes soft X-ray NS atmosphere models, and thus no constraints on mass and radius can be derived. However, for Aql X–1 during flares in

the quiescent state, no correlation between the hard and soft components was found (Cackett et al. 2010; Coti Zelati et al. 2014). From the two-component spectral fit models, the nonthermal component can be attributed to the X-ray variability, even though the thermal component variation cannot be completely ruled out. During the Aql X–1 outburst in 2010, the interaction between the magnetic field and the stellar rotation may explain the fast decay time back to quiescence. The post-outburst quiescent X-ray luminosity correlates with the strength of the nonthermal emission, due to residual accretion (Campana et al. 2014). The post-outburst quiescent states have been observed also with *Swift* in 2012, 2013, and 2015 (Waterhouse et al. 2016). In these cases, the spectrum was fitted with the addition of a significant hard spectral component in 2012, and with pure thermal emission in 2013 and 2015 (Waterhouse et al. 2016). Interestingly, even if during the 2012 and 2013 outbursts the spectral components were different, the soft component (i.e., NS temperature) evolved from the outburst to the quiescent states with the same trend. It can be summarized that for Aql X–1 the thermal component is deep crustal cooling. This conclusion should be confirmed by future observations because of the low signal-to-noise ratio of the *Swift* spectra.

To infer the NS mass and radius, high signal-to-noise ratio *Chandra* and *XMM-Newton* data have been obtained for six NS qLMXBs, located in the globular clusters M13, M28, M30, ω Cen, NGC 6397, and NGC 6304 (Guillot et al. 2013). The soft X-ray spectra were fitted with a pure hydrogen atmosphere model, NSATMOS. The NS spectra have been fitted simultaneously, assuming one radius value for all NSs. The determined radius is $9.1^{+1.3}_{-1.5}$ km (Guillot et al. 2013). This value has been marginally improved to 9.4 ± 1.2 km by increasing the exposure of the M30 and ω Cen *Chandra* observations (Guillot & Rutledge 2014) and increased to $10.3^{+1.2}_{-1.1}$ km by using updated distance measurements to globular clusters (Guillot 2016). Combining the sample of these six qLMXB sources, with the addition of six LMXBs exhibiting PRE bursts and assuming an NS mass of $1.5 M_{\odot}$, a radius of $10.8^{+0.5}_{-0.4}$ km is found (Özel et al. 2016). These works exclude two EOSs for the matter above the nuclear saturation density, MS0 (Müller & Serot 1996) and PAL (Prakash et al. 1988) at the 99% confidence level (c.l.; Guillot et al. 2013; Guillot & Rutledge 2014), and prefer the EOS of AP4 (Akmal & Pandharipande 1997), especially for low-mass NSs (Özel et al. 2016). We note that the observed high NS masses up to $\sim 2 M_{\odot}$, as well as low NS masses down to $\sim 1 M_{\odot}$, may constrain the EOSs too (Demorest et al. 2010; Antoniadis et al. 2013; Falanga et al. 2015; Li et al. 2015).

1.3. The Source Aql X–1

Aql X–1 is a transient LMXB, hosting an NS orbiting around a main-sequence K4 spectral type companion (Callanan et al. 1999; Chevalier et al. 1999; Mata Sánchez et al. 2017).

In the past few decades, the source was monitored with many X-ray instruments (e.g., Campana et al. 1998, 2013). Aql X–1 is known to host a fast spinning pulsar of ~ 550.27 Hz with an orbital period of ~ 18.97 hr, exhibiting frequent outbursts and type I X-ray bursts (Campana et al. 1998, 2013; Casella et al. 2008; Galloway et al. 2008). The source distance has been estimated in the range of 4–6.5 kpc, based on the companion star filling its Roche lobe to produce the frequently observed outbursts (Rutledge et al. 2001b). Recently, it has been revised

to 6 ± 2 kpc, and the uncertainty mainly comes from our limited knowledge on the companion star type and radius (see Mata Sánchez et al. 2017, for more details). In our simulations, we use a distance in the range of 4–6.5 kpc (see Section 4).

From high-resolution spectroscopy, obtained with *XMM-Newton*/RGS, a hydrogen column density of $N_{\text{H}} = (5.21 \pm 0.05) \times 10^{21} \text{ cm}^{-2}$ has been measured by Pinto et al. (2013). These authors measured nitrogen K edge, iron L2 and L3 edge, and oxygen K edge, which led to a model-independent estimate of the hydrogen column density. This parameter is fundamental for determining the NS mass and radius from its quiescent spectra (see Section 3.1), which is applied to the case of qLMXBs located in globular clusters. This is because the distance to globular clusters is accurately known through optical observations, and the nonthermal emission in these objects contributes negligibly to the total flux, limiting the impact on the determination of the NS mass and radius. In the case of Aql X–1, the nonthermal component contributes by $\geq 15\%$ to the total source flux (Campana et al. 2014; Coti Zelati et al. 2014). Coti Zelati et al. (2014) compared the contributions of the power-law component in the quiescent spectra of the source and concluded that it is due to residual accretion heating the NS atmosphere. Hence, the variations of the thermal temperature and the PL normalization are enough to account for the residual accretion.

The qLMXBs hosted in globular clusters are observed to emit almost a pure thermal emission (nonthermal component flux less than 5%), being good study cases to measure the mass and radius (Guillot et al. 2013; Heinke et al. 2014; Bogdanov et al. 2016). However, open questions should be still better explored in the quiescent spectral method, such as the atmosphere composition of NSs and the origin of nonthermal emission. Both the PRE burst and qLMXB methods have a few undetermined parameters, such as a color correction factor, or the atmosphere composition. Moreover, at present, no LMXB in a globular cluster has high signal-to-noise ratio spectra and PRE bursts simultaneously. In this paper, we analyze Aql X–1, which has distance estimation, PRE bursts from *RXTE*, and high signal-to-noise ratio spectra from *XMM-Newton* and *Chandra*. We constrain the mass and radius of Aql X–1 for the first time with the above-mentioned methods and investigate the consistency between them.

In Section 2 we report the Aql X–1 data from *Chandra*, *XMM-Newton*, and *RXTE* observations. In Section 3 we show the time-resolved PRE bursts and quiescent spectrum results. The derived mass and radius are reported in Section 4, and its uncertainties are discussed in Section 5. Finally, we draw our conclusions on the determined Aql X–1 mass and radius in Section 6.

2. Observations and Data

We analyzed the quiescent spectra obtained by *Chandra* and *XMM-Newton* observations. The X-ray bursts were studied by exploiting *RXTE* data. Our total data set includes 15 quiescent *Chandra* observations, 5 quiescent *XMM-Newton* observations, and 14 *RXTE* pointings during which several PRE bursts have been detected. The *Chandra* and *XMM-Newton* data are obtained from previous studies (Rutledge et al. 2001a; Cackett et al. 2011; Campana et al. 2014). The logs of all used observations are shown in Tables 1 and 2.

Table 1
Quiescent Observations of Aql X–1

ObsID <i>XMM-Newton</i>	Exposure Time (ks)	Detector	Net Count Rate (counts s ⁻¹ [0.5–10 keV])	
0085180401	7.20	MOS1	0.096 ± 0.004	
		MOS2	0.100 ± 0.004	
0085180501	4.91	PN	0.331 ± 0.009	
		14.42	MOS1	0.093 ± 0.003
		MOS2	0.100 ± 0.003	
0112440101	11.31	PN	0.309 ± 0.006	
		2.46	MOS1	0.058 ± 0.005
0112440301	7.08	MOS2	0.059 ± 0.005	
		MOS1	0.049 ± 0.003	
0112440401	13.40	MOS2	0.053 ± 0.003	
		MOS1	0.047 ± 0.002	
		MOS2	0.048 ± 0.002	
<i>Chandra</i>				
708	6.63	ACIS-S	0.182 ± 0.005	
709	7.79	ACIS-S	0.092 ± 0.003	
710	7.39	ACIS-S	0.126 ± 0.004	
711	9.25	ACIS-S	0.123 ± 0.004	
3484	6.60	ACIS-S	0.162 ± 0.005	
3485	6.96	ACIS-S	0.182 ± 0.005	
3486	6.49	ACIS-S	0.343 ± 0.007	
3487	5.94	ACIS-S	0.094 ± 0.004	
3488	6.51	ACIS-S	0.087 ± 0.004	
3489	7.13	ACIS-S	0.079 ± 0.003	
3490	6.94	ACIS-S	0.104 ± 0.004	
7629	9.87	ACIS-S	0.092 ± 0.003	
12457	6.36	ACIS-S	0.258 ± 0.006	
12458	6.36	ACIS-S	0.147 ± 0.005	
12459	6.36	ACIS-S	0.158 ± 0.005	

2.1. *Chandra*

The (Weisskopf et al. 2000) data reduction was performed by using CIAO v4.6 with standard procedures. We reprocess the data CHANDRA_REPRO⁹ indicated in Table 1 to create level-2 event files. The SPECEXTRACT tool was used to extract the source spectra from a circled region centered on the object with a radius of 4'' (8 pixels); the background spectra were carefully extracted from a nearby source-free region with a radius of 10'' (20 pixels) located on the same CCD. ObsID 12456 was heavily piled up, and thus we excluded these data in our analysis (see Campana et al. 2014, for more details). The MKACISRMF and MKARF scripts were used to generate the response matrix (rmf) and ancillary response files (arf). To account for the absolute flux calibration, we added 3% systematic uncertainties in the energy range 0.5–10 keV.

2.2. *XMM-Newton*

We made use only of *XMM-Newton* (Jansen et al. 2001) data in image mode in order to exploit the high-resolution energy spectra. The data reduction was carried out by using the emchain and epchain tools included in the *XMM-Newton Science Analysis System*. Following the standard data reduction threads,¹⁰ we filtered the EPIC data with the FLAG = 0 option and retained all events with pattern 0–4 (0–12) for the pn (MOS) detector(s). The source spectra were extracted from a circle with a radius of 32''

⁹ <http://cxc.harvard.edu/ciao/threads/data.html>

¹⁰ <http://www.cosmos.esa.int/web/xmm-newton/sas-threads>

Table 2
Log of the Aql X-1 *RXTE* PRE Bursts Observations Analyzed in This Paper and Spectral Properties of the Bursts

ObsID	Burst No. ^a	Touchdown Flux (10^{-7} erg cm $^{-2}$ s $^{-1}$)	Peak Flux (10^{-7} erg cm $^{-2}$ s $^{-1}$)	K (0.1–0.7 F_{TD}) ^b ($(\text{km}/10 \text{ kpc})^2$)	kT_{TD} ^c (keV)	PCU ^d
20092-01-05-00	#1 (5)	1.20 ± 0.08	1.20 ± 0.08	278 ± 30	2.52 ± 0.02	All
20092-01-05-030	#2 (6)	0.62 ± 0.09	0.74 ± 0.15	280 ± 41	2.28 ± 0.06	All
20098-03-08-00	#3 (4)	1.20 ± 0.06	1.20 ± 0.06	321 ± 101	2.66 ± 0.04	All
40047-03-02-00	#4 (10)	1.29 ± 0.07	1.29 ± 0.07	272 ± 26	2.52 ± 0.03	0, 2, 3, 4
40047-03-06-00	#5 (11)	1.18 ± 0.16	1.19 ± 0.78	290 ± 29	2.82 ± 0.07	0, 2, 4
40048-01-02-00	#6 (13)	0.57 ± 0.02	0.66 ± 0.02	290 ± 49	2.61 ± 0.02	0, 1, 2, 3
50049-02-13-01	#7 (19)	0.73 ± 0.11	0.84 ± 0.06	376 ± 113	2.42 ± 0.07	0, 2, 3, 4
60054-02-03-03	#8 (25)	0.94 ± 0.06	0.95 ± 0.25	304 ± 38	2.16 ± 0.03	0, 1, 2, 3
60429-01-06-00	#9 (28)	1.21 ± 0.08	1.21 ± 0.08	391 ± 124	2.59 ± 0.03	0, 2, 3, 4
70069-03-02-03	#10 (29)	0.64 ± 0.06	0.73 ± 0.06	339 ± 77	2.38 ± 0.04	0, 2, 3
92438-01-02-01	#11	1.03 ± 0.13	1.18 ± 0.07	584 ± 158	2.77 ± 0.07	0, 2, 4
93405-01-03-07	#12	0.76 ± 0.06	1.08 ± 0.06	277 ± 33	2.20 ± 0.03	0, 1, 2
94076-01-05-02	#13	1.00 ± 0.21	1.08 ± 0.09	242 ± 45	2.19 ± 0.03	1, 2, 4
96440-01-09-07	#14	1.06 ± 0.09	1.06 ± 0.09	291 ± 55	2.72 ± 0.05	2

Notes.

^a Burst No. marked in this work. The burst No. marked in Galloway et al. (2008) is given in parentheses. The PRE bursts in the last four observations were identified recently.

^b The mean value and standard deviation of apparent angular size in the range 0.1–0.7 F_{TD} during the cooling tail. Here, $F_{\text{TD}} = 1.06 \times 10^{-7}$ erg cm $^{-2}$ s $^{-1}$.

^c The blackbody temperature at the touchdown moment.

^d The active Proportional Counter Units (PCUs) during the burst epoch.

Table 3
Fitting to the $F-K^{-1/4}$ and $kT_{\text{bb}}-K^{-1/4}$ Relations

Obs_ID	Burst No.	F_{Edd} (10^{-7} erg cm $^{-2}$ s $^{-1}$)	A ($((R(1+z)/D)^{-1/2})$)	χ^2_{red} (dof) ^a	χ^2_{red} (dof) ^b
20092-01-05-00	#1	1.18 ± 0.10	0.163 ± 0.002	13.07(13)	6.09(13)
20092-01-05-030	#2	0.62 ± 0.01	0.168 ± 0.001	1.12(23)	1.37(23)
20098-03-08-00	#3	1.06 ± 0.26	0.155 ± 0.012	12.86(11)	8.75(11)
40047-03-02-00	#4	1.10 ± 0.15	0.158 ± 0.009	16.97(16)	8.13(16)
40047-03-06-00	#5	1.18 ± 0.01	0.158 ± 0.002	3.43(10)	1.69(10)
40048-01-02-00	#6
50049-02-13-01	#7	0.84 ± 0.01	0.161 ± 0.001	1.90(22)	1.38(22)
60054-02-03-03	#8	0.64 ± 0.16	0.154 ± 0.014	14.97(11)	5.69(11)
60429-01-06-00	#9	0.80 ± 0.31	0.142 ± 0.014	15.74(16)	7.58(16)
70069-03-02-03	#10	0.64 ± 0.01	0.160 ± 0.001	1.11(21)	0.65(21)
92438-01-02-01	#11	0.85 ± 0.04	0.133 ± 0.002	10.34(28)	10(28)
93405-01-03-07	#12	0.83 ± 0.06	0.164 ± 0.005	11.99(32)	6.14(32)
94076-01-05-02	#13	1.02 ± 0.02	0.160 ± 0.002	8.45(25)	7.85(25)
96440-01-09-07	#14	1.01 ± 0.09	0.163 ± 0.003	4.63(3)	4.88(3)

Notes.

^a The reduced χ^2 and degree of freedom from the fitting of $F-K^{-1/4}$.

^b The reduced χ^2 and degree of freedom from the fitting of $kT_{\text{bb}}-K^{-1/4}$.

and 28" for the pn and MOS, respectively. The background pn and MOS spectra were extracted from a circular source-free region with a radius of 100" (the background and source extraction region were located in the same CCD). We used the RMFGEN and ARFGEN to generate the response matrices file and the ancillary response file for each observation. We added a systematic uncertainty of 3% in the energy range 0.5–10 keV in order to take into account the instrument absolute flux calibrations. The quiescent spectra and the best-fit models are shown in Figure 1 (see Section 3.1 for more details).

2.3. *RXTE*

(Jahoda et al. 1996) observed over 1000 X-ray bursts from hundreds of LMXBs during its scientific operations (Galloway et al. 2008). Thanks to its large collecting area and relatively

wide energy band coverage, *RXTE* is well suited to carry out a time-resolved spectral analysis of the X-ray bursts. We found 14 PRE bursts from Aql X-1 in the type I X-ray burst catalog published by Galloway et al. (2008) and the later works by Chen et al. (2013) and Kajava et al. (2014). We note that only one PRE burst (No. 11) occurred while the source was in a hard state based on its color-color diagram position (Chen et al. 2013; Kajava et al. 2014). The detailed *RXTE* observations are reported in Table 2.

The burst time-resolved spectra were extracted from the cleaned science event files, and dead-time effects were corrected following standard procedures. For each PRE burst, a 16 s spectrum prior to the burst was extracted and used as background (thus including the contribution from the source persistent emission, the diffuse X-ray background, and the

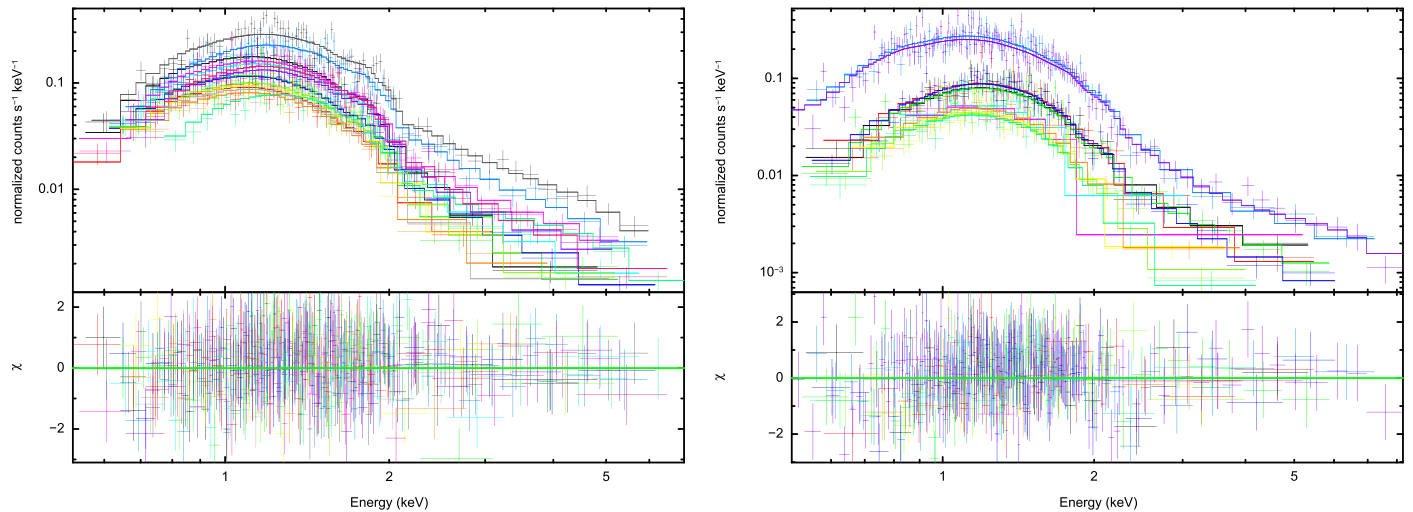


Figure 1. Left panel: Aql X-1 spectra observed by *Chandra*. Right panel: *XMM-Newton* spectra. We plot the absorbed spectrum of Aql X-1 fit with an absorbed, TBABS, NS thermal atmosphere, NSATMOS, and power-law model. The N_{H} value, source distance, and NS mass and radius are fixed at $5.21 \times 10^{21} \text{ cm}^{-2}$, 5 kpc, $1.4 M_{\odot}$, and 10 km, respectively. The lower panel shows the residual between the data and the model.

instrument background). The exposure of the time-resolved spectra (3–22 keV) during each of the bursts was chosen in such a way that each spectrum was characterized by a similar signal-to-noise ratio. In particular, we used an exposure time of 2 s when the source count rate was $\leq 1500 \text{ counts s}^{-1}$, 1 s for count rates of $\leq 3000 \text{ counts s}^{-1}$, 0.5 s for count rates of $\leq 6000 \text{ counts s}^{-1}$, and 0.25 s for count rates of $> 6000 \text{ counts s}^{-1}$. We rebinned all spectra in order to have at least 20 photons in each energy bin (see Section 3.2). A systematic error of 0.5% was applied to *RXTE*/PCA spectra, which corresponds to the uncertainty in the response matrix (Shaposhnikov et al. 2012). The uncertainties in the burst spectral parameters are given at 1σ c.l. for a single parameter.

All 14 PRE type I X-ray burst spectra were best fitted with an absorbed, TBABS, and a blackbody, BBODYRAD, model. No hard X-ray excesses were recorded in these bursts (see also Galloway et al. 2008). For some of the spectra, a Gaussian component was used to model the broad iron line around 6.4 keV seen in *RXTE* data. We fixed the Gaussian bandwidth at 0.3 keV to take into account the limited energy resolution of the instrument (Jahoda et al. 2006). Given that we were not able to constrain the hydrogen column density value, N_{H} (as the PCA bandpass starts above 3 keV), we fixed it to the value of $5.21 \times 10^{21} \text{ cm}^{-2}$ (see Section 3.1). We display the results in Figure 2.

The bolometric flux is defined as (Galloway et al. 2008)

$$F = 1.076 \times 10^{-11} \left(\frac{kT_{\text{bb}}}{1 \text{ keV}} \right)^4 \text{ K erg cm}^{-2} \text{ s}^{-1}, \quad (6)$$

where the uncertainty was estimated by the general equation of the propagation of the errors.

Burst No. 6 (ObsID 40048-01-02-00) is a peculiar event, as it has been identified as a PRE burst by Galloway et al. (2008) but not by Chen et al. (2013) or by Kajava et al. (2014). In addition, as its time-solved spectra frequently show null values, we excluded it for the Aql X-1 mass and radius determination procedure. For completeness, we just show this peculiar burst with a time bin of 2 s to avoid null bin values in Figure 2. Burst No. 11 shows a flux excess during its cooling tail, i.e., occurring $t = 20$ s from the onset of the burst. This flux excess

is highlighted in red in Figure 3 and excluded for the following analysis in this work.

3. Results

3.1. The Quiescent Spectra

The spectral analysis was carried out using XSPEC version 12.8.2 (Arnaud 1996). We studied in detail the quiescent X-ray spectra of Aql X-1 in the energy range 0.5–10 keV, using *Chandra*/ACIS-S and *XMM-Newton*/PN/MOS data. We grouped all *Chandra* and *XMM-Newton* spectra in order to have at least 20 photons in each energy bin. We summarize in Table 1 all the analyzed spectra. To account for the soft thermal and hard emission components, we fitted all the spectra with an absorbed NS atmosphere, NSATMOS, adding also a power-law component. The free parameters are the hydrogen column density N_{H} , NS atmosphere temperature, distance to the source, NS mass and radius, power-law index Γ , and power-law normalization. We assume throughout the spectral fits that during the quiescent state the whole NS surface is radiating. Therefore, the NSATMOS emission fraction parameter was set to unity. We used the XSPEC absorption model, TBABS, with the WILM abundances (Wilms et al. 2000). All uncertainties in the spectral parameters are given at 1σ c.l. for a single parameter.

To compare the consistency due to the absolute flux calibration between *XMM-Newton*/PN/MOS and *Chandra*/ACIS-S spectra (see, e.g., Güver et al. 2016), we first fitted separately all the *XMM-Newton*/PN/MOS and *Chandra*/ACIS-S spectra. For the NSATMOS model we let free to vary the atmosphere temperature and fixed the NS mass and radius to the canonical values ($M = 1.4 M_{\odot}$, $R = 10$ km). The source distance was first set to the lower limit of 4 kpc and afterward to the upper limit of 6.25 kpc. For the lower and upper source distance values, the best fits provided an absorption column density of $N_{\text{H}} = (6.1 - 5.1) \pm 0.1 \times 10^{21} \text{ cm}^{-2}$ and a power-law photon index $\Gamma = (1.2 - 0.7) \pm 0.2$ with a $\chi^2_{\text{red}}/\text{d.o.f.} = 0.9/481$ and $0.9/591$ for *XMM-Newton*/PN/MOS and *Chandra*/ACIS-S spectra, respectively. For the joint *XMM-Newton* data we include a normalization constant in the fit to take into account the uncertainties in the cross-calibrations of the instruments and the source variability (the data are not

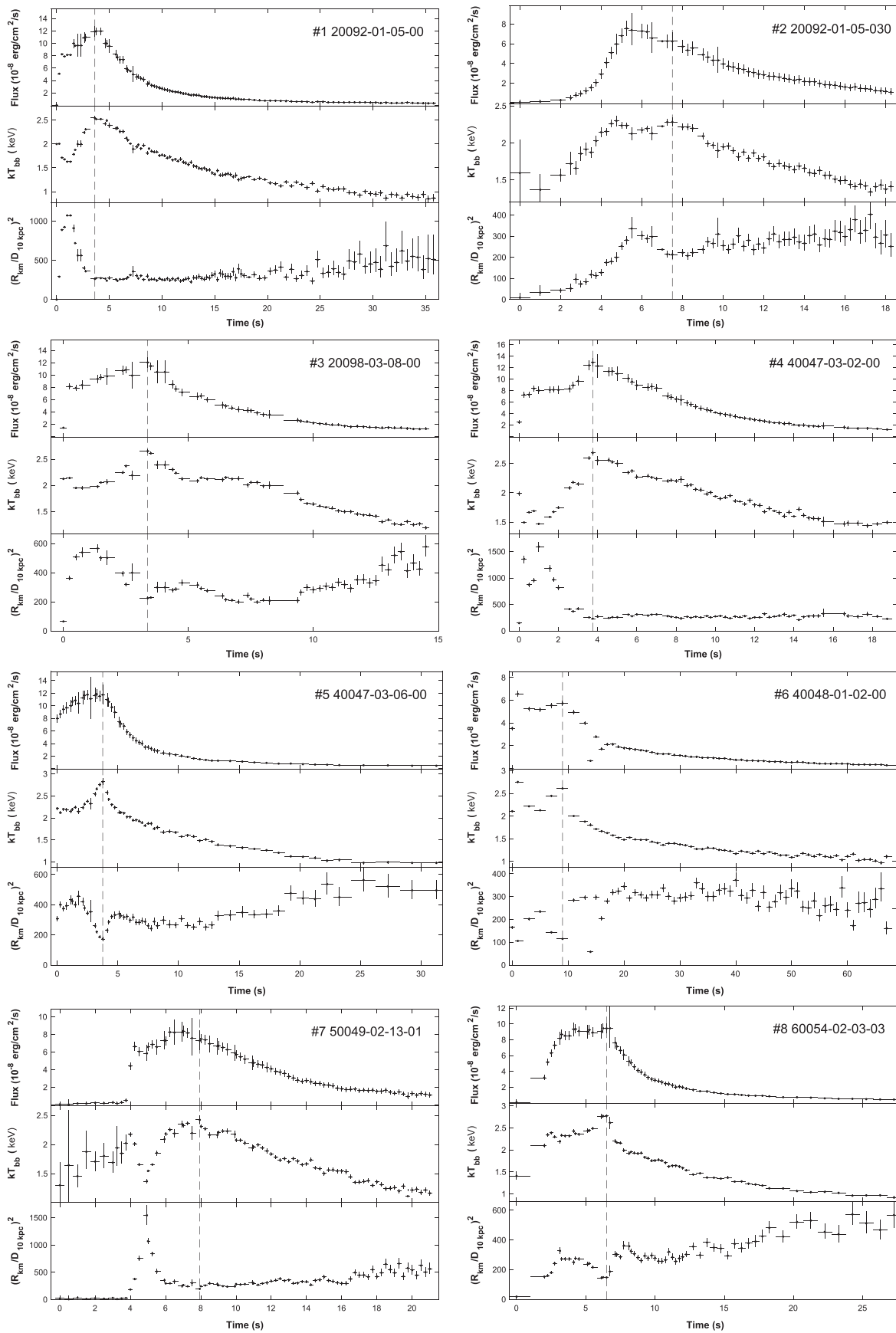


Figure 2. Time-resolved spectroscopic results from all 14 analyzed PRE bursts. We show the inferred flux from the best-fit blackbody model (top panels), the blackbody temperature (middle panels), and the blackbody normalization (bottom panels). The vertical dashed line marks the touchdown moment in each plot.

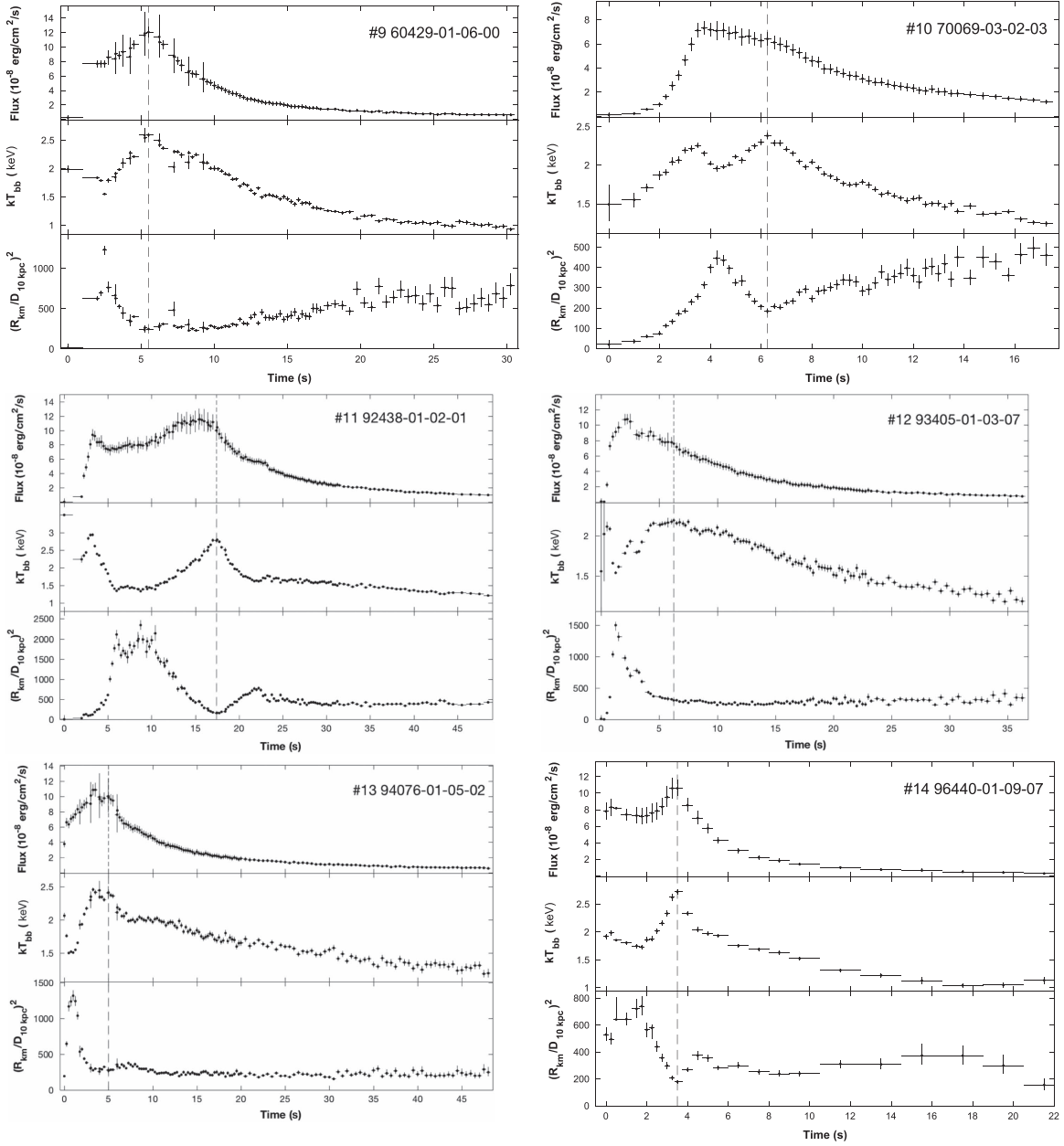


Figure 2. (Continued.)

covering strictly the same time interval). In this fit, the normalization of the MOS data was fixed to unity as a reference, while the normalization of the PN data was found to be 1.1 ± 0.2 . Similar values were found also for the combined *XMM-Newton*/PN/MOS and *Chandra*/ACIS-S spectra fit with a $\chi^2_{\text{red}}/\text{d.o.f.} = 0.9/1073$. In this case the normalization constant was fixed to unity for the *Chandra* data, while the normalization constant of the PN and MOS data was found to be 0.9 ± 0.1 , for both instruments. The quiescent spectra from *Chandra* and *XMM-Newton* and their best-fitting models are displayed in Figure 1.

Although the fits were all formally acceptable, the NS mass and radius have to be free parameters. We thus fixed throughout this work the model-independent reported hydrogen column density at $5.21 \times 10^{21} \text{ cm}^{-2}$ (Pinto et al. 2013; see Section 1.3). We then fitted again the *Chandra* and *XMM-Newton* spectra separately to investigate the consistency of the

mass and radius constraints. The distance was set at $5 \pm 0.25 \text{ kpc}$. The NS atmosphere temperature is a free parameter for all spectra, while the power-law indices were tied together and free to change for *Chandra* and *XMM-Newton* spectra. To consider now a mass and radius skewed distribution, we apply the Goodman–Weare algorithm of Markov Chain Monte Carlo (MCMC; e.g., Goodman & Weare 2010; Guillot et al. 2013). This simulation procedure is implemented as CHAIN in the XSPEC package. For each of the 200 chains, the length was 2×10^6 . The first 20% of the simulated data were burned. The mass and radius contours are displayed in Figure 4.

The mass and radius of the NS constrained from *Chandra* and *XMM-Newton* are consistent with each other. However, *Chandra* spectra provide tighter constraints on the NS mass and radius for Aql X–1 than *XMM-Newton*. The most likely explanation is that *Chandra* observed Aql X–1 more frequently

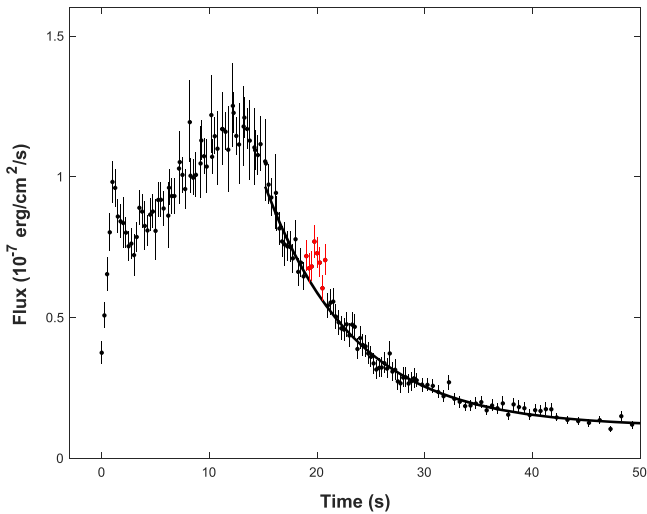


Figure 3. PRE burst No. 11 light curve. The flux excess during the decay phase is highlighted with red data points. The black solid line is the exponential best fit to the decay phase. The fitted function is $\text{Flux} = ae^{bt} + c$, and the weighted Nelder–Mead method is applied, where $a = 5.34 \times 10^{-7}$, $b = -0.12$, $c = 1.4 \times 10^{-8}$.

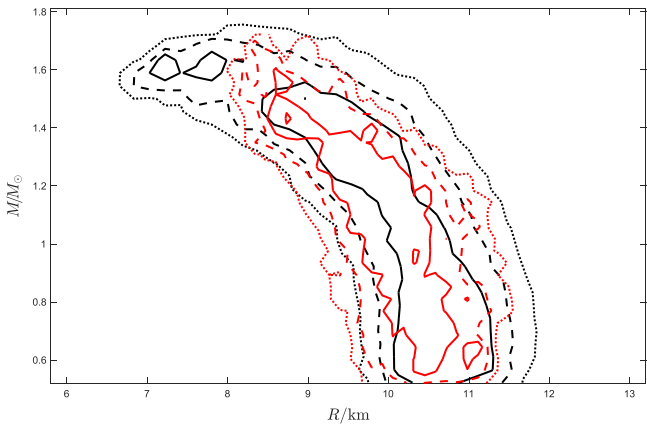


Figure 4. Consistency of the M – R relation between the *Chandra* and *XMM-Newton* observations. The 1σ , 2σ , 3σ confidence regions of the mass and radius in Aql X–1 from *Chandra* (red contours) and *XMM-Newton* (black contours). The distance is 5 ± 0.25 kpc, and the N_{H} is fixed at $5.21 \times 10^{21} \text{ cm}^{-2}$. For more details, please see Section 4.

than *XMM-Newton* as listed in Table 1. The total number of photons collected by *Chandra* is about 1.34 times larger than that of *XMM-Newton*, so the signal-to-noise ratio of the *Chandra* spectra is higher than that of the *XMM-Newton* spectra shown in Figure 1. We note that the nicely overlapping mass–radius contours are not obtained if we set the hydrogen column density at $N_{\text{H}} = 6.1 \times 10^{21} \text{ cm}^{-2}$. We thus preferred to use the model-independent determined N_{H} value of $5.21 \times 10^{21} \text{ cm}^{-2}$.

We directly combined the *Chandra* and *XMM-Newton* observations together and derived the mass–radius relation in Section 4.

3.2. PRE Bursts in Aql X–1

3.2.1. Theory-driven Approach

For each PRE burst we fitted the F – $K^{-1/4}$ relation obtained from the observations with the theoretical model No. 8 from Suleimanov et al. (2012), where $\log g = 14.3$ and $X = 0.7343$, $Y = 0.2586$, $Z = 4.02 \times 10^{-3}$ are the abundances of

hydrogen, helium, and metals, respectively. The purpose of the selected abundance is that the burst cooling atmosphere probably has similar composition to its main-sequence companion star. We consider first that the model-predicted PRE burst Eddington flux, F_{Edd} , is free to vary between 0.8 and 1.2 times the touchdown flux, and then that only cooling tail fluxes larger than F_{TD}/e are considered (Poutanen et al. 2014). We obtain the best-fit results with the regression method by minimizing the function (see, e.g., Deming 2011; Suleimanov et al. 2017)

$$\chi^2 = \sum_{i=1}^{N_{\text{obs}}} \left[\frac{(Af_c - K_i^{-1/4})^2}{(\sigma_{K_i^{-1/4}})^2} + \frac{(F_{\text{Edd}}\ell - F_i)^2}{\sigma_{F_i}^2} \right]. \quad (7)$$

The K_i and F_i are the i th data points in the cooling tail, where $\sigma_{K_i^{-1/4}}$ and σ_{F_i} are the corresponding errors. The theoretical relation ℓ – f_c is adapted from Suleimanov et al. (2012). The errors of the data are taken into account in both directions. The term in square brackets is the square of the normalized distance from the i th data to the model curve ℓ – f_c .

The best-fit values and uncertainties of A and F_{Edd} are obtained by the bootstrap method. The fit to the kT – f_c relation is carried out in the similar way. We found that 11 PRE bursts out of 13 fit the kT_{bb} – $K^{-1/4}$ tracks better, with smaller χ_{red}^2 , compared to the F – $K^{-1/4}$ trend. This confirms the finding that the data are best fit with the relation kT_{bb} – $K^{-1/4}$ (see also Özel & Psaltis 2015). The bursts with relatively good fits are burst No. 11, i.e., the hard-state PRE burst (see Figure 5), and four PRE bursts in the soft state (see Figure 6). Three of them (burst nos. 2, 7, 10) have acceptable χ_{red}^2 values (both $\chi_{\text{red}}^2 < 2$); however, the touchdown fluxes are in the range of $(6.2$ – $7.3) \times 10^{-8} \text{ erg cm}^{-2} \text{ s}^{-1}$, which are only $\lesssim 60\%$ of the brightest bursts. If we use these samples to constrain the mass and radius of Aql X–1, it will underestimate the mass measurement. For the hard-state PRE burst (No. 11), the data can follow the trend of the model, but the χ_{red}^2 are larger. The theoretical model No. 8 from Suleimanov et al. (2012) is not the only one to fit the data well. For the same abundance, the theoretical predictions are insensitive to the $\log g$ as explained in Suleimanov et al. (2012). All fit results are listed in Table 3.

3.2.2. Data-driven Approach

Based on the best data selection criteria introduced by Özel et al. (2015, 2016), a PRE burst, which can be used to determine the NS mass and radius, should satisfy at least two conditions. First, the touchdown flux should be the brightest ones among all samples, taking also the uncertainties into account. Second, the photospherical radius at the expansion phase should be evidently larger than the asymptotic value at the cooling tail. The No. 11 PRE burst has larger mean value and standard derivation than other selected bursts, which may be contaminated by the X-ray excess during the decay (see Figure 3). For burst No. 9, the blackbody normalization increased during the cooling tail; hence, these two bursts are not included in our samples. Overall, in our sample, PRE burst Nos. 1, 4, 12, 13, and 14 follow the two conditions.

We only extracted the blackbody normalization in the range of $0.1 \sim 0.7 F_{\text{TD}}$ (Özel et al. 2016), and the mean values are listed in Table 2. The other selected PRE bursts have roughly the same blackbody normalizations, which are different from the noisy results extracted in the range of $(5 \times 10^{-9} - F_{\text{TD}}) \text{ erg cm}^{-2} \text{ s}^{-1}$

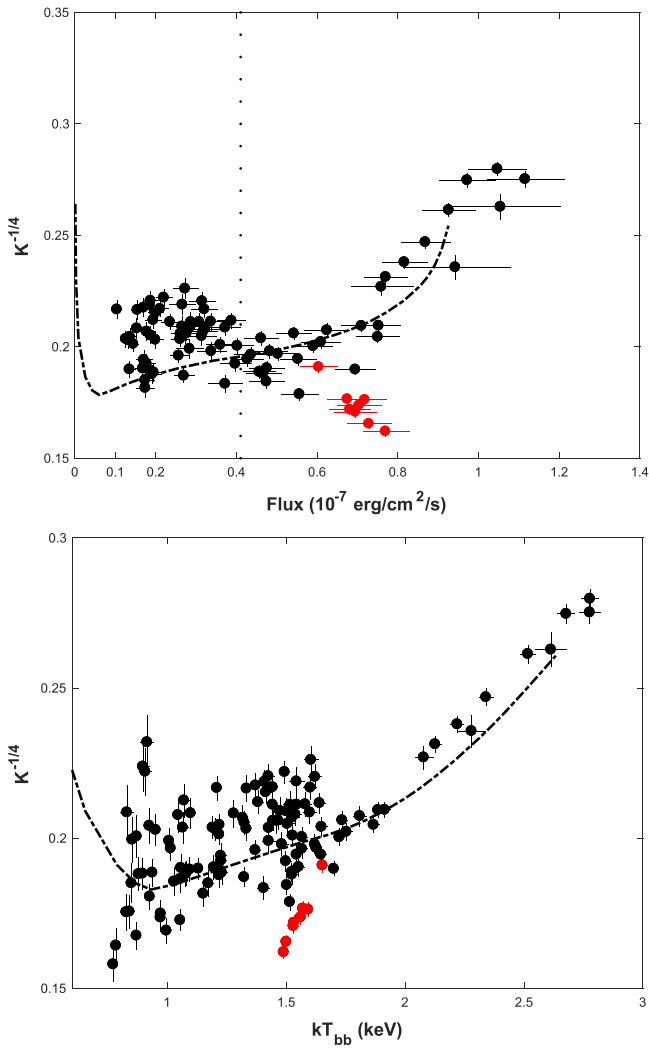


Figure 5. The $F-K^{-1/4}$ (top panel) and $kT_{\text{bb}}-K^{-1/4}$ tracks of the hard-state PRE burst (No. 11) in Aql X-1. The red filled circles are the flux excesses as shown in Figure 3, which are excluded in our fits.

from all X-ray bursts, i.e., PRE and non-PRE bursts (Güver et al. 2012). Therefore, we obtain the touchdown flux, apparent angular size K , touchdown temperature kT_{TD} , and their errors from the weighted mean and standard deviations of the selected samples, which are $(1.06 \pm 0.10) \times 10^{-7} \text{ erg cm}^{-2} \text{ s}^{-1}$, $279 \pm 30 \text{ (km/10 kpc)}^2$, and $2.51 \pm 0.09 \text{ keV}$, respectively, and are applied in our calculations.

4. Aql X-1 Mass and Radius

The $M-R$ values of Aql X-1 were independently constrained from the quiescent spectra observed by *Chandra* and *XMM-Newton*, as well as from the PRE bursts detected by *RXTE*.

As the distance to Aql X-1 was not accurately measured, we divided the distance into $4 \pm 0.25 \text{ kpc}$, $4.5 \pm 0.25 \text{ kpc}$, $5 \pm 0.25 \text{ kpc}$, $5.5 \pm 0.25 \text{ kpc}$, and $6 \pm 0.25 \text{ kpc}$, with a box-car prior distribution for both methods, and simulated them separately. From the quiescent spectra, we first run the MCMC simulations with the upper and lower limits of N_{H} , which are 5.16×10^{21} and $5.26 \times 10^{21} \text{ cm}^{-2}$, respectively. The results are in well agreement with each other. We thus fix N_{H} at $5.21 \times 10^{21} \text{ cm}^{-2}$ to limit the computational time. The power-law index was tied for *Chandra* and *XMM-Newton* spectra and

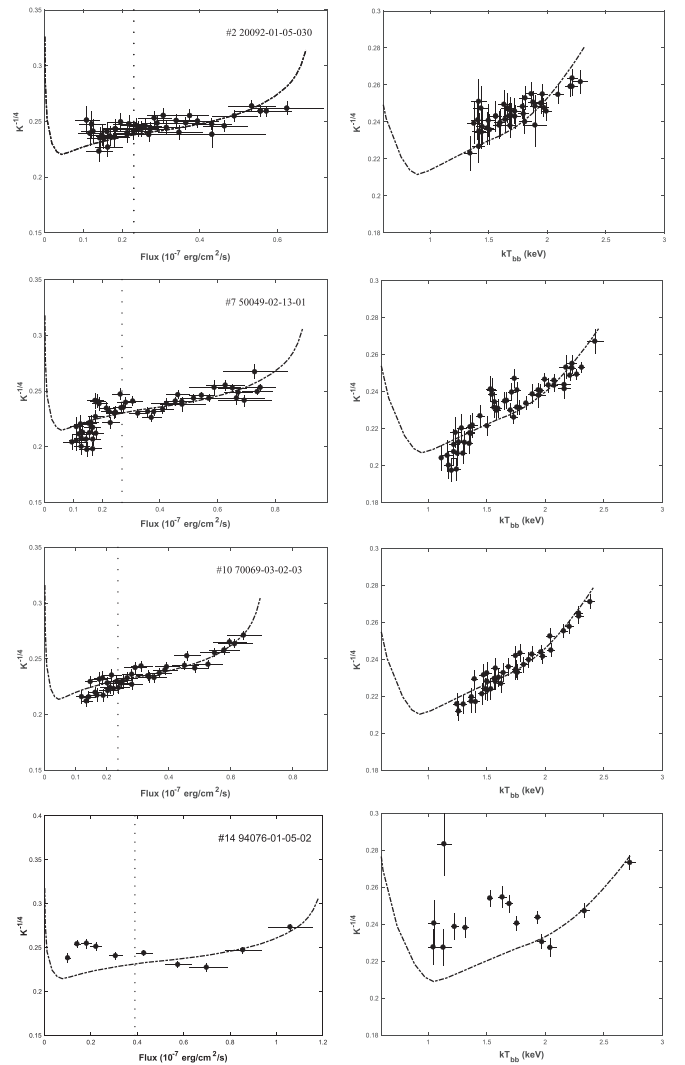


Figure 6. The $F-K^{-1/4}$ (left panels) and $kT_{\text{bb}}-K^{-1/4}$ (right panels) tracks and their best-fit model of the soft-state PRE bursts (Nos. 2, 7, 10, 14, from top to bottom) in Aql X-1. The vertical dotted line in the left panels presents the fitting truncated at F_{TD}/e (see Poutanen et al. 2014, for more details).

free to vary. In addition, the NS atmosphere temperature, mass, radius, power-law normalization, and distance were set as free parameters during the fit. For each of the 200 chains, the length was 2×10^6 . The 20% of the steps prior to the chains were burned. We also used the `xspec_emcee`¹¹ program, developed by Jeremy Sanders, to perform the MCMC simulations. The confidence regions of mass and radius are very similar to those obtained with the chain command in `XSPEC`. The convergence of the MCMC was also verified, as the length of each chain is much larger (>600) than the autocorrelation time of the mass and radius series and the chain of simulated parameters showed no significant trends or excursions.

From PRE bursts, we adopted the Bayesian approach to measure the mass and radius of the NS. In Equation (5), the corrected touchdown flux and apparent angular size were applied based on Equations (3) and (4). We chose prior Gaussian distributions for kT_{TD} , K , and F_{TD} and prior flat distributions for distance, hydrogen mass fraction, and color correction factor, which are expressed as $D \sim U[D - dD, D + dD]$,

¹¹ https://github.com/jeremysanders/xspec_emcee

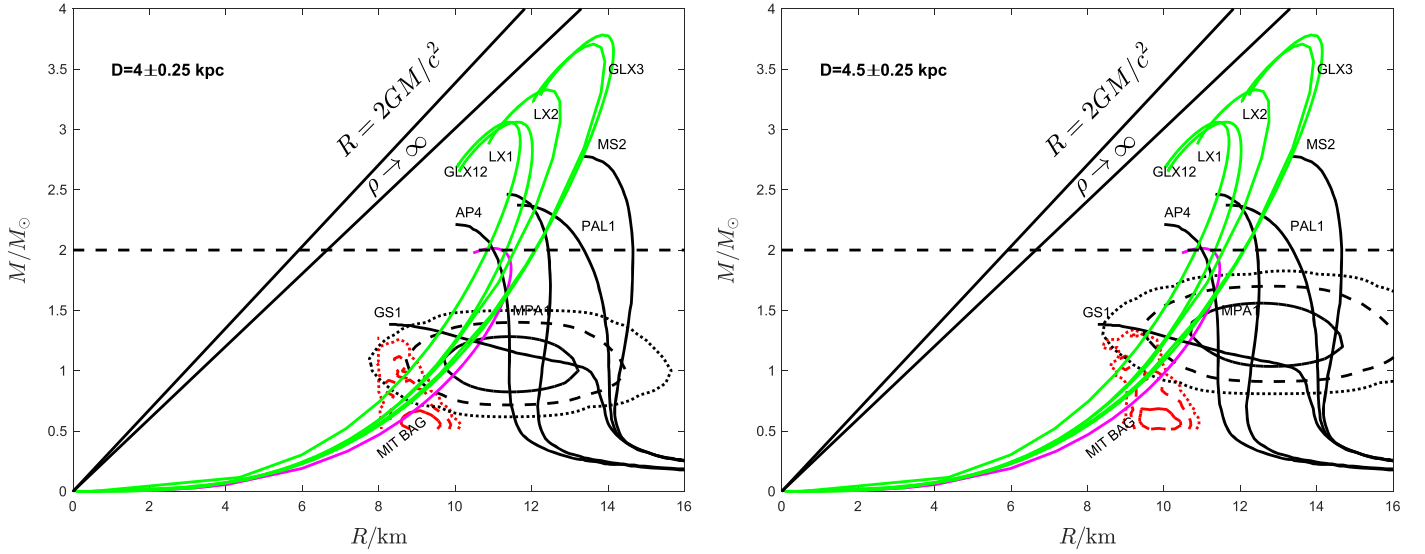


Figure 7. Mass and radius of Aql X-1. The contours are obtained from PRE bursts (nearly horizontal black contours) and quiescent spectra (skewed red contours), respectively. The solid, dashed, and dotted contours represent the 1σ , 2σ , and 3σ c.l., respectively. The distance is set as 4 ± 0.25 kpc (left panel) and 4.5 ± 0.25 kpc (right panel). In both panels, the dashed line labels two observed near $2 M_{\odot}$ NSs. The two black straight lines show the constraints from the general relatively (GR) and the central density limit, respectively. Theoretical mass–radius relations were predicted for several NS EOS models, which are marked as GS1 (Glendenning & Schaffner-Bielich 1999), AP4 (Akmal & Pandharipande 1997), MPA1 (Müther et al. 1987), PAL1 (Prakash et al. 1988), MS2 (Müller & Serot 1996), GLX123 (Guo et al. 2014), and LX12 (Lai & Xu 2009; Lai et al. 2013). The purple dot-dashed line represents the bare strange stars obtained from the MIT bag model EOS with the bag constant $57 \text{ MeV}/\text{fm}^3$. The first five EOSs are gravity bound, while the rest of them are self-bound on the surface.

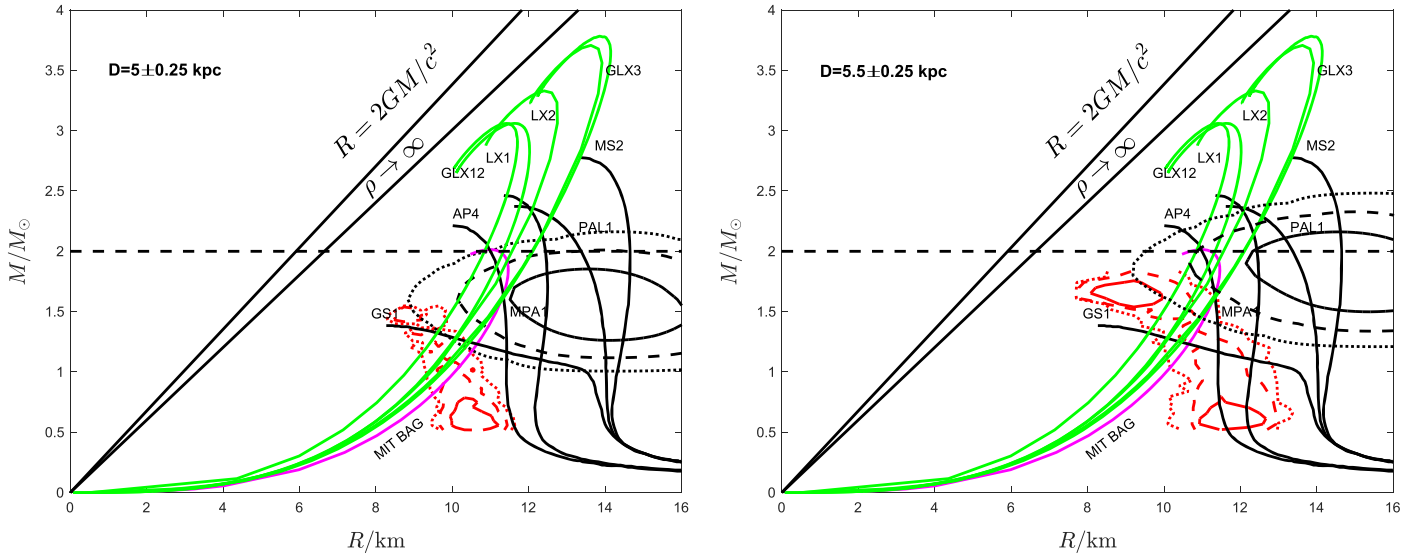


Figure 8. Similar to Figure 7, but the distance is 5 ± 0.25 kpc (left panel) and 5.5 ± 0.25 kpc (right panel).

$X \sim U[0.3, 1]$, and $f_c \sim U[1.35, 1.45]$, respectively. The NS mass and radius obtained from the PRE burst method are shown as nearly horizontal black contours in Figures 7 and 8. We only displayed the results for distances as high as 5.5 ± 0.25 kpc, as no overlapping region exists combining these results with the qLMXB method at higher distances.

The mass and radius of Aql X-1 are shown in Figures 7 and 8. The horizontal and skewed contours are obtained by using the results from PRE bursts and quiescent spectra, respectively. The distance and its uncertainty are taken into account in the simulations. In each case, the uncertainty is 0.25 kpc, while the distance spans the range 4 – 5.75 kpc. From these results, we found that the overlapped M – R confidence regions are always consistent with the strange matter EOSs (e.g., quark star and quark-cluster star; Lai & Xu 2009; Lai et al.

2013; Guo et al. 2014), and only the conventional NS EOS (Akmal & Pandharipande 1997) for the distance of 5.25 – 5.75 kpc. In addition, no confidence regions are overlapped between quiescent spectra and PRE bursts when the distance is above 5.75 kpc. Hence, we can roughly estimate a distance range of 4 – 5.75 kpc.

5. Discussions

5.1. Nonuniform Emission due to Residual Accretion?

The power-law component in quiescent spectra shows that the residual accretion may occur during the quiescent state. In our fitting procedure, we assume a uniform temperature on the NS surface. If the accreted matter has a nonuniform distribution in a long timescale, our assumption could be questionable.

However, assuming that the timescale for the accreted matter to diffuse over the surface is τ_{diff} in a random-walk approximation, one has $R \sim N^{1/2} r_L$, where R is the stellar radius, $r_L \sim 3 \times 10^{-2} (B/10^8 \text{ G})^{-1} \text{ cm}$ the Larmor radius, and $N = \tau_{\text{diff}}/\tau_c$ the number of collisions within the collision timescale $\tau_c \sim 10^{-14} \text{ s}$ (e.g., Goldston & Rutherford 1995; Xu 2014). If $B \sim 10^8 \text{ G}$ and the density of the heated matter is on the order of 10^2 g cm^{-3} , we have $\tau_{\text{diff}} \sim 10 \text{ s}$, which is much shorter than the characteristic time of heat conduction and cooling. The accreted matter is thus likely to diffuse quickly and heat almost the entire NS surface if the stellar magnetic field is weak ($B \sim 10^8 \text{ G}$ on the surface). Furthermore, the pulse fraction was only about 2% even in a continuous accretion process (Casella et al. 2008), which implies a negligible inhomogeneous temperature distribution. We thus conclude that the NS surface is uniformly emitting, even if the residual accretion occurs during quiescence.

5.2. The Possible Reasons Why Overlapping M - R Relations at 1σ c.l. Do Not Exist

We notice that there are no overlapping M - R relations between the PRE bursts and qLMXB results at 1σ c.l. This can be explained in at least three scenarios. First, we assumed a pure hydrogen NS atmosphere in the NSATMOS model. However, the atmosphere on the surface of Aql X-1 should be composed of a mix of hydrogen and helium, as its companion is a main-sequence star. Second, we corrected the fast rotation effects of Aql X-1 in the PRE burst method, but these theoretical calculations are still not taken into account in quiescent NS atmosphere models. The combination of fast rotation and a hydrogen and helium mixed NS atmosphere in a refined spectral model could help us in understanding better the quiescent spectra of Aql X-1. Third, we assume that the photosphere expands in spherical symmetry. However, the diversity of the mean cooling area implies that the photosphere expansion might be asymmetric, which biases the NS mass and radius measurements.

6. Summary

For the first time the mass and radius of Aql X-1 were constrained by PRE bursts and quiescent spectra simultaneously. As these two methods are completely independent, the NS mass and radius can give better constraints.

Fourteen PRE bursts were observed in Aql X-1, and only one of them during the source hard state. Poutanen et al. (2014) suggested that only PRE bursts in the hard state can be used to determine the NS mass and radius, as the accretion rate is relatively low in the hard state and the accretion disk is not expected to produce obvious effects on the cooling tracks. Indeed, the cooling track of Aql X-1 in the hard state follows the prediction of Suleimanov et al. (2011, 2012) with large χ_{red}^2 . We found, in any case, that the three soft-state PRE bursts followed the theoretical prediction of the F - $K^{-1/4}$ and $kT_{\text{bb}}-K^{-1/4}$ relations, but the touchdown fluxes are apparently smaller than the brightest ones. In addition, Özel et al. (2015) proposed that the rapid evolution of the color correction factor could be missed at touchdown owing to limitations of *RXTE*.



From the quiescent data observed by *Chandra* and *XMM-Newton*, we fitted the spectra with an absorbed hydrogen atmosphere emission component plus a hard power-law component. We used the Goodman-Weare algorithm of MCMC to simulate the NS mass and radius for various prior

distance distributions. The NS mass and radius in Aql X-1 are shown in Figures 7 and 8. Ten EOSs were also plotted to illustrate the constraints of Aql X-1. Once the results from the PRE bursts observed by *RXTE* are combined with the quiescent spectra observed by *Chandra* and *XMM-Newton*, the mass and radius of Aql X-1 are found to be compatible with the strange matter EOSs (Lai & Xu 2009; Lai et al. 2013; Guo et al. 2014) and the conventional NS EOS (Akmal & Pandharipande 1997). Moreover, we also concluded that the distance to Aql X-1 should be in the range of 4.0–5.75 kpc because no overlapped M - R confidence region exists when higher distances are considered.

The EOSs of a compact star could be strictly tested by very high mass NSs and very low mass NSs (Li et al. 2015), as well as accurate measurements of NS mass and radius. In this work, we applied simultaneously two well-established methods for Aql X-1, which could effectively reduce the mass and radius uncertainties (see Figures 7 and 8). Precious distance measurements from optical observations (such as the Thirty Meter Telescope) could help in obtaining tighter constraints on the NS EOSs. Better constraints on the NS EOSs are expected to be obtained in the future by the advanced capabilities of eXTP (Zhang et al. 2016), which will be able to measure simultaneously the NS pulse profile with high accuracy and its quiescent spectrum with larger signal-to-noise ratio and collect both PRE bursts and gravitational redshift measurements.

We thank the anonymous referee for comments and suggestions that significantly improved our manuscript. Z.L. is supported by the Swiss Government Excellence Scholarships. Z.L. thanks the International Space Science Institute for the hospitality during his visiting, L. Zampieri for providing his Xspec table model generously, and E. Bozzo for carefully reading this manuscript. This work is supported by the National Natural Science Foundation of China (11225314, 11173024), Hunan Provincial NSF 2017JJ3310, and the Strategic Priority Research Program on Space Science of the Chinese Academy of Sciences (XDA04010300). This research has made use of data obtained from the High Energy Astrophysics Science Archive Research Center (HEASARC), provided by NASA's Goddard Space Flight Center. The FAST FELLOWSHIP is supported by the Special Funding for Advanced Users, budgeted and administrated by the Center for Astronomical Mega-Science, CAS.

ORCID iDs

Zhaosheng Li  <https://orcid.org/0000-0003-2310-8105>
 Maurizio Falanga  <https://orcid.org/0000-0003-3095-6065>
 Jinlu Qu  <https://orcid.org/0000-0002-9796-2585>
 Renxin Xu  <https://orcid.org/0000-0002-6595-2956>

References

- Akmal, A., & Pandharipande, V. R. 1997, *PhRvC*, **56**, 2261
- Antoniadis, J., Freire, P. C. C., Wex, N., et al. 2013, *Sci*, **340**, 448
- Arnaud, K. A. 1996, in ASP Conf. Ser. 101, *Astronomical Data Analysis Software and Systems V*, ed. G. H. Jacoby & J. Barnes (San Francisco, CA: ASP), 17
- Bauböck, M., Psaltis, D., & Özel, F. 2015, *ApJ*, **811**, 144
- Beloborodov, A. M. 2002, *ApJL*, **566**, L85
- Bernardini, F., Cackett, E. M., Brown, E. F., et al. 2013, *MNRAS*, **436**, 2465
- Bogdanov, S., Heinke, C. O., Özel, F., & Güver, T. 2016, *ApJ*, **831**, 184
- Bogdanov, S., Rybicki, G. B., & Grindlay, J. E. 2007, *ApJ*, **670**, 668
- Brown, E. F., Bildsten, L., & Rutledge, R. E. 1998, *ApJL*, **504**, L95

- Cackett, E. M., Brown, E. F., Miller, J. M., & Wijnands, R. 2010, *ApJ*, **720**, 1325
- Cackett, E. M., Fridriksson, J. K., Homan, J., Miller, J. M., & Wijnands, R. 2011, *MNRAS*, **414**, 3006
- Callanan, P. J., Filippenko, A. V., & Garcia, M. R. 1999, *IAUC*, **7086**, 3
- Campana, S., Brivio, F., Degenaar, N., et al. 2014, *MNRAS*, **441**, 1984
- Campana, S., Coti Zelati, F., & D'Avanzo, P. 2013, *MNRAS*, **432**, 1695
- Campana, S., Israel, G. L., Stella, L., Gastaldello, F., & Mereghetti, S. 2004, *ApJ*, **601**, 474
- Campana, S., Stella, L., Mereghetti, S., et al. 1998, *ApJL*, **499**, L65
- Casella, P., Altamirano, D., Patruno, A., Wijnands, R., & van der Klis, M. 2008, *ApJL*, **674**, L41
- Chakrabarty, D., Tomsick, J. A., Grefenstette, B. W., et al. 2014, *ApJ*, **797**, 92
- Chen, Y.-P., Zhang, S., Zhang, S.-N., et al. 2013, *ApJL*, **777**, L9
- Chevalier, C., Ilovaisky, S. A., Leisy, P., & Patat, F. 1999, *A&A*, **347**, L51
- Coti Zelati, F., Campana, S., D'Avanzo, P., & Melandri, A. 2014, *MNRAS*, **438**, 2634
- Cottam, J., Paerels, F., & Mendez, M. 2002, *Natur*, **420**, 51
- Cottam, J., Paerels, F., Méndez, M., et al. 2008, *ApJ*, **672**, 504
- D'Angelo, C. R., Fridriksson, J. K., Messenger, C., & Patruno, A. 2015, *MNRAS*, **449**, 2803
- Deming, W. E. 2011, *Statistical Adjustment of Data* (New York: Dover)
- Demorest, P. B., Pennucci, T., Ransom, S. M., Roberts, M. S. E., & Hessels, J. W. T. 2010, *Natur*, **467**, 1081
- Ebisuzaki, T., Sugimoto, D., & Hanawa, T. 1984, *PASJ*, **36**, 551
- Falanga, M., Bozzo, E., Lutovinov, A., et al. 2015, *A&A*, **577**, A130
- Galloway, D. K., Muno, M. P., Hartman, J. M., Psaltis, D., & Chakrabarty, D. 2008, *ApJS*, **179**, 360
- Gendreau, K. C., Arzoumanian, Z., & Okajima, T. 2012, *Proc. SPIE*, **8443**, 844313
- Glendenning, N. K., & Schaffner-Bielich, J. 1999, *PhRvC*, **60**, 025803
- Goldston, R. J., & Rutherford, P. H. 1995, *Introduction to Plasma Physics* (Boca Raton, FL: CRC Press)
- Goodman, J., & Weare, J. 2010, *Commun. Appl. Math. Comput. Sci.*, **5**, 65
- Guillot, S. 2016, *MmSAI*, **87**, 521
- Guillot, S., & Rutledge, R. E. 2014, *ApJL*, **796**, L3
- Guillot, S., Rutledge, R. E., & Brown, E. F. 2011, *ApJ*, **732**, 88
- Guillot, S., Servillat, M., Webb, N. A., & Rutledge, R. E. 2013, *ApJ*, **772**, 7
- Guo, Y.-J., Lai, X.-Y., & Xu, R.-X. 2014, *ChPhC*, **38**, 055101
- Güver, T., Özel, F., Marshall, H., et al. 2016, *ApJ*, **829**, 48
- Güver, T., Psaltis, D., & Özel, F. 2012, *ApJ*, **747**, 76
- Haakonsen, C. B., Turner, M. L., Tacik, N. A., & Rutledge, R. E. 2012, *ApJ*, **749**, 52
- Hartman, J. M., Patruno, A., Chakrabarty, D., et al. 2008, *ApJ*, **675**, 1468
- Heinke, C. O., Cohn, H. N., Lugger, P. M., et al. 2014, *MNRAS*, **444**, 443
- Heinke, C. O., Rybicki, G. B., Narayan, R., & Grindlay, J. E. 2006, *ApJ*, **644**, 1090
- Jahoda, K., Markwardt, C. B., Radeva, Y., et al. 2006, *ApJS*, **163**, 401
- Jahoda, K., Swank, J. H., Giles, A. B., et al. 1996, *Proc. SPIE*, **2808**, 59
- Jansen, F., Lumb, D., Altieri, B., et al. 2001, *A&A*, **365**, L1
- Kajava, J. J. E., Nättälä, J., Latvala, O.-M., et al. 2014, *MNRAS*, **445**, 4218
- Lai, X. Y., Gao, C. Y., & Xu, R. X. 2013, *MNRAS*, **431**, 3282
- Lai, X. Y., & Xu, R. X. 2009, *MNRAS*, **398**, L31
- Lattimer, J. M. 2012, *ARNPS*, **62**, 485
- Leahy, D. A. 2004, *ApJ*, **613**, 517
- Leahy, D. A., Morsink, S. M., Chung, Y.-Y., & Chou, Y. 2009, *ApJ*, **691**, 1235
- Lewin, W. H. G., van Paradijs, J., & Taam, R. E. 1993, *SSRv*, **62**, 223
- Li, Z.-S., Qu, Z.-J., Chen, L., et al. 2015, *ApJ*, **798**, 56
- Madej, J., Joss, P. C., & Różańska, A. 2004, *ApJ*, **602**, 904
- Majczyna, A., Madej, J., Joss, P. C., & Różańska, A. 2005, *A&A*, **430**, 643
- Mata Sánchez, D., Muñoz-Darias, T., Casares, J., & Jiménez-Ibarra, F. 2017, *MNRAS*, **464**, L41
- Miller, M. C., & Lamb, F. K. 2016, *EPJA*, **52**, 63
- Morsink, S. M., Leahy, D. A., Cadeau, C., & Braga, J. 2007, *ApJ*, **663**, 1244
- Müller, H., & Serot, B. D. 1996, *NuPhA*, **606**, 508
- Müther, H., Prakash, M., & Ainsworth, T. L. 1987, *PhLB*, **199**, 469
- Özel, F. 2006, *Natur*, **441**, 1115
- Özel, F., Güver, T., & Psaltis, D. 2009, *ApJ*, **693**, 1775
- Özel, F., & Psaltis, D. 2015, *ApJ*, **810**, 135
- Özel, F., Psaltis, D., & Guver, T. 2015, arXiv:1509.02924
- Özel, F., Psaltis, D., Güver, T., et al. 2016, *ApJ*, **820**, 28
- Pechenick, K. R., Ftaclas, C., & Cohen, J. M. 1983, *ApJ*, **274**, 846
- Pinto, C., Kaastra, J. S., Costantini, E., & de Vries, C. 2013, *A&A*, **551**, A25
- Poutanen, J., & Gierliński, M. 2003, *MNRAS*, **343**, 1301
- Poutanen, J., Nättälä, J., Kajava, J. J. E., et al. 2014, *MNRAS*, **442**, 3777
- Prakash, M., Lattimer, J. M., & Ainsworth, T. L. 1988, *PhRvL*, **61**, 2518
- Psaltis, D., & Özel, F. 2014, *ApJ*, **792**, 87
- Psaltis, D., Özel, F., & Chakrabarty, D. 2014, *ApJ*, **787**, 136
- Rutledge, R. E., Bildsten, L., Brown, E. F., Pavlov, G. G., & Zavlin, V. E. 2001a, *ApJ*, **551**, 921
- Rutledge, R. E., Bildsten, L., Brown, E. F., Pavlov, G. G., & Zavlin, V. E. 2001b, *ApJ*, **559**, 1054
- Shaposhnikov, N., Jahoda, K., Markwardt, C., Swank, J., & Strohmayer, T. 2012, *ApJ*, **757**, 159
- Sidoli, L., Parmar, A. N., & Oosterbroek, T. 2005, *A&A*, **429**, 291
- Strohmayer, T., & Bildsten, L. 2006, in *New Views of Thermonuclear Bursts*, ed. W. H. G. Lewin & M. van der Klis (Cambridge: Cambridge Univ. Press), **113**
- Suleimanov, V., Poutanen, J., & Werner, K. 2011, *A&A*, **527**, A139
- Suleimanov, V., Poutanen, J., & Werner, K. 2012, *A&A*, **545**, A120
- Suleimanov, V. F., Poutanen, J., Nättälä, J., et al. 2017, *MNRAS*, **466**, 906
- Sztajno, M., Fujimoto, M. Y., van Paradijs, J., et al. 1987, *MNRAS*, **226**, 39
- Taylor, J. H. 1992, *RSPTA*, **341**, 117
- Waterhouse, A. C., Degenaar, N., Wijnands, R., et al. 2016, *MNRAS*, **456**, 4001
- Watts, A., Espinoza, C. M., Xu, R., et al. 2015, in *Advancing Astrophysics with the Square Kilometre Array (AASKA14)*, **43**
- Webb, N. A., & Barret, D. 2007, *ApJ*, **671**, 727
- Weisberg, J. M., Nice, D. J., & Taylor, J. H. 2010, *ApJ*, **722**, 1030
- Weisskopf, M. C., Tananbaum, H. D., Van Speybroeck, L. P., & O'Dell, S. L. 2000, *Proc. SPIE*, **4012**, 2
- Wilms, J., Allen, A., & McCray, R. 2000, *ApJ*, **542**, 914
- Xu, R.-X. 2014, *RAA*, **14**, 617
- Zampieri, L., Campana, S., Turolla, R., et al. 2001, *A&A*, **378**, L5
- Zampieri, L., Turolla, R., Zane, S., & Treves, A. 1995, *ApJ*, **439**, 849
- Zavlin, V. E., Pavlov, G. G., & Shibanov, Y. A. 1996, *A&A*, **315**, 141
- Zhang, S. N., Feroci, M., Santangelo, A., et al. 2016, *Proc. SPIE*, **9905**, 99051Q